PAPER

Check for updates

ZnO-templated hollow amorphous carbon: oxygen adsorption and doping synergy for enhanced ORR catalysis†

Guandong Wang,[a] Yizhi Yin,[a] Chenfeng Lin,[a] Shixiong Min [ID][a] and Jinfu Ma [ID] *[a,b]

In pursuit of highly active zinc–air battery (ZAB) catalysts, nitrogen doping has proven key to enhancing carbon-based non-metallic catalysts' performance in the oxygen reduction reaction (ORR). This study employed a novel method to synthesize variously sized ZnO materials coated with ZIF-8. Notably, smaller particle sizes correlated with reduced activation energy. ZnO-12, the smallest variant, fully carbonized at 800 °C, resulting in zinc ion evaporation and the formation of an amorphous carbon nano-hollow structure, ZIF8/ZnO-12. This material showcased remarkable ORR properties, with an onset potential of 0.9 V (*vs.* RHE) and a Tafel slope of 71.4 mV dec^{-1}, surpassing the benchmark Pt/C catalyst and exhibiting excellent stability. Moreover, in ZAB tests, ZIF8/ZnO-12 achieved a specific capacity of 816 mA h g^{-1}, outperforming Pt/C. DFT calculations indicate that under alkaline conditions, nitrogen-doped carbon materials containing adsorbed oxygen and doped oxygen exhibit lower catalytic activation energy for the ORR, which is beneficial for accelerating the ORR. This research provides valuable insights into designing more efficient carbon-based non-metallic catalysts for ZABs.

1. Introduction

Precious metals and metal oxides are widely utilized catalysts in fuel cells. However, metal-based catalysts are usually expensive, less durable, less selective, and have a negative impact on the environment. Carbon-based nonmetallic catalysts have received increasing interest due to their excellent electrocatalytic properties. Many heteroatom-doped carbon materials exhibit high ORR activity. Of these catalysts, nitrogen-doped carbon materials are particularly effective in nonmetallic catalysis.[1–3] The fundamental reason for this efficacy lies in their atomic radii and electronegativity; the atomic radius of N atoms (0.74 Å) is close to that of carbon atoms (0.77 Å), and the electronegativity of N atoms (3.04) is higher than that of carbon atoms (2.55). As a result, N atoms would then be readily doped into the carbon material, thereby altering the electron distribution in the carbon-based network. Among the N doping types, pyridine N is considered to be the most

effective for ORR.[4–6] It was shown that the concentration of pyridine N directly controls the ORR activity and its decisive role was emphasized by Kondo *et al.*[7] Pyridine N atoms usually prefer to occupy defects or edges of carbon materials.[7–9] However, it is more difficult to obtain sufficiently high concentrations of selectively doped pyridine nitrogen atoms due to the relatively low edge densities and defects in current carbon materials.[10,11] Therefore, in order to solve the current challenge of achieving high concentrations of selectively doped pyridine nitrogen atoms in carbon materials, a new carbon skeleton needs to be explored as an ideal substrate for pyridine nitrogen doping.

Carbon materials are crystallographically divided into graphitic carbon and amorphous carbon. In amorphous carbon,[12–15] amorphous carbon refers to a turbulent disordered structure in which the periodic arrangement of carbon molecular layers is no longer continuous and different degrees of stacking dislocations occur. Usually, disordered structures have more defects, and the presence of defects causes an increase in the number of catalytically active sites.[16] Cao *et al.*[17] demonstrated that nitrogen-doped amorphous carbon will also be more active and stable than graphitized carbon, and that graphitization of metal elements and carbon is not a necessary factor for the use of nitrogen-doped carbon as a non-precious metal catalyst for ORR. Based on the advantages of amorphous carbon, this paper, from this material, the direct carbonization of MOFs has recently become the main-

[a]*School of Materials Science and Engineering, North Minzu University, Yinchuan 750021, China. E-mail: ma_jinfu@nun.edu.cn*
[b]*Research Center of Silicon Target and Silicon-Carbon Negative Material Engineering Technology, School of Materials Science and Engineering, North Minzu University, Yinchuan 750021, China*

stream choice.[18,19] The template method[19–21] is also used to increase the specific area of surface and thus improve the catalytic activity of amorphous carbon. Qian's group synthesized a hierarchical hollow carbon nanomaterials (HNCT-CNTs) through one-step pyrolysis on bimetallic ZIFZn/Co precursors, which are enriched with Co-Nx sites. Zou's group[22] investigated the effects of carbonization temperature and ZIF-8 particle size on the structural and capacitive properties of carbon materials and concluded that when the carbonization temperature exceeds 800 °C, the carbon materials have a high degree of graphitization. However, as the volatilization temperature of zinc oxide is 907 °C,[23] maintaining the amorphous nature of carbon materials requires reducing the thermal activation energy of zinc oxide.[24,25] Relationship between treatment activation energy and particle size, Cui *et al.*[26] determined the thermal decomposition curves of nanomaterials with different size of grains by using a thermal analyzer and calculated their thermal decomposition activation energies by combining the isotropic conversion rate method with multiple heating and the iterative method, and concluded that the thermal decomposition activation energy reduces with the particle size, and that the apparent activation energy has a linearity relationship with the inverse of the particle size. Similar studies were conducted by Saibal *et al.*[27] The kinetics of non-isothermal thermal breakdown of carbonate powders was calculated using a method close to the accurate solution of the modified Arrhenius equation, and the same conclusion was reached, the apparent energy of activation for the decomposition of $CaCO_3$ reduced with the average size of the calcium carbonate nanoparticles. Beyond $CaCO_3$ materials, Jiang *et al.*[28] investigated the influence of particle size on the pyrolysis of polystyrene and found that the activation energy increases as the size of the particles increases for the same conversion rate. All the above experiments demonstrated that the smaller particle size can reduce the pyrolysis activation energy.

Herein, a controlled pipe diameter modulation strategy was employed to synthesize fine zinc oxide nanotubes.[29,30] Zinc oxide served as a template in conjunction with ZIF-8, and the resulting composite was subjected to carbonization at a specific temperature. This approach facilitated the volatilization of zinc oxide while concurrently maintaining the amorphous nature of carbon. For the change of the obvious oxygen-related peaks in the experimental results XPS, combined with the prominent ORR catalytic activity, the atomic model of pyridine N-binding O-substituted graphene is designed and DFT theoretical calculations are carried out to explore the more essential reasons for the catalytic properties of the material.

2. Experimental section

2.1 Chemicals

Anhydrous ethanol (CH_3CH_2OH), potassium hydroxide (KOH) and ammonia (NH_3 H_2O) were obtained from Sinopharm Chemical Reagent Co., Ltd. Zinc nitrate ($Zn(NO_3)_2 \cdot 6H_2O$), PEG 2000 ($HO(CH_2CH_2O)_nH$), 2-methylimidazole ($C_4H_6N_2$) and

N,N-dimethylformamide(DMF) (C_3H_7NO) were obtained from Aladdin Biochemical Technology Co., Ltd. Nafion and Pt/C (20 wt%) were purchased from Sigma-Aldrich.

2.2 Preparation of catalysts

2.2.1 Preparation of ZnO. Add 0.9 g of PEG with a molecular weight of 2000 and 3 g of $Zn(NO_3)_2$ $6H_2O$ to 375 ml of deionized water at room temperature and stir for 15 minutes. The mixture was placed in an ultrasonic cleaner and 1 M NH_3 H_2O was added dropwise until the pH was 10. Three sets of solutions were obtained by repeating the above method, and then they were placed in three thermostatic magnetic stirrers at 80 °C and stirred for 8 hours, 12 hours and 14 hours. The precipitate obtained by filtration was washed three times with deionized water and anhydrous ethanol, respectively. This operation is to remove PEG residues and nitrate ions. Finally, the samples were dried in a vacuum oven at 60 °C for 12 hours. The products obtained were noted as ZnO-8, ZnO-12, and ZnO-14, each exhibiting distinct nanostructures such as nanoflowers, nanorods, and nanotubes, as depicted in Fig. S1.†

2.2.2 Synthesis of ZnO catalysts with different diameters attached to ZIF-8. A mixture of 160 mL of deionized water and 480 mL of DMF was dissolved with 6.6 g of $C_4H_6N_2$ by stirring, and the above method was repeated to obtain three sets of solutions. To each of the three solutions, 0.84 g of ZnO-8, ZnO-12, ZnO-14 was added and processed in an ultrasonic cleaner for 30 minutes. Subsequently, the three sets of solutions were placed in an electrically heated blast dryer at 60 °C to maintain the temperature for 48 hours. The resulting powder was cleaned three times with ethanol and then placed in a vacuum drying oven and dried at 60 °C for 12 hours. The prepared samples were put into a crucible and transferred to a vacuum tube furnace. Prior to carbonization, the furnace was evacuated by blowing in nitrogen and parameterized to heat up to 200 °C for 2 hours at 5 °C min^{-1}, then to 800 °C for 5 hours at the same rate. The resulting products were noted as ZIF8/ZnO-8, ZIF8/ZnO-12, and ZIF8/ZnO-14.

2.3 Preparation of electrocatalysts

Experiments related to electrochemical correlation tests were performed on a three-electrode system controlled by a CHI 760E electrochemical workstation. Prior to measurement, the solution was gassed with O_2/N_2 for 30 minutes to saturate the solution with gas. A saturated Hg/HgO electrode was used as the reference electrode and the counter electrode was a graphite rod. O_2/N_2 saturated 0.1 M KOH aqueous solution was used as the electrolyte. The working electrode was prepared by dispersing 10 mg of sample in a mixture of 0.15 ml of deionized water and 0.35 ml of ethanol to which 10 μl of Nafion was added. Ultrasonication was applied until a homogeneous ink suspension was formed. The obtained 10 μL of ink was uniformly coated on the freshly polished glassy carbon rotating disk electrode and dried at room temperature to be used as a working electrode. A commercial Pt/C catalyst ink (Alpha, 20 wt% Pt/C) was prepared for the comparison group using the

same method. To fabricate the cathode electrode for zinc-air batteries, 80 μL of the ink was carefully drop-cast onto polytetrafluoroethylene-coated carbon cloth (WOS1002). The coated cloth was then air-dried for 30 minutes at 85 °C.

3.   Results and discussion

Fig. 1(a) displays the XRD patterns of ZnO nanorods and ZnO nanotubes synthesized at different preparation times (8, 12, and 14 hours) under the same thermal deposition temperature. In this experimental setup, the catalysts, namely ZIF8/ZnO-8 and ZIF8/ZnO-14, obtained by attaching ZIF-8 to the nanorods/nanotubes for 8 and 14 hours, respectively, were compared with the standard JCPDS card (PDF#89-1397).[31,32] The diffraction angles at 31.74°, 34.38°, 36.21°, 47.48°, 56.53°, 62.76°, 66.30°, 67.87°, 69.00°, and 76.87° were identified, corresponding to the (100), (002), (101), (102), (110), (103), (200), (112), (201), and (202) crystal planes of ZnO. The resulting ZnO nanomaterials exhibited a hexagonal wurtzite structure, as evidenced by sharp and narrow peaks in the XRD pattern, indicative of a certain degree of crystallinity. However, the XRD of the post-synthesis pyrolysis of ZIF-8-attached 12 hours nanotubes (ZIF-8/ZnO-12) shows a broad diffraction peak near 21°, indicating a low degree of graphitization, which is predominantly carbon with an amorphous structure, and does not contain any peaks of residual ZnO or other impurities of $Zn(OH)_2$. The generation of Nitrogen-rich carbon nanotubes by ZnO-attached porous ZIF-8 can significantly increase the number of the effective active site of ORR. It was found that these nitrogen-activated carbon nanotubes have many defects, a defective structure that is typically found in nitrogen-doped graphene materials, and can generate a high number of active sites, which can improve electrocatalytic activity.

In Raman testing analysis, two broad peaks in each group of samples are divided into four peaks based on Gaussian distribution for simulation, as shown in Fig. 1(b). The sp^2 carbon is represented by $D_8 = 1348.86$ cm^{-1} $D_{12} = 1351.76$ cm^{-1} $D_{14} = 1345.76$ cm^{-1} $G_8 = 1589.7$ cm^{-1} $G_{12} = 1583.91$ cm^{-1} $G_{14} = 1571.91$ cm^{-1}, and the sp^3 carbon is represented by $E_8 = 1179$ cm^{-1} $E_{12} = 1167.91$ cm^{-1} $E_{14} = 1175.5$ cm^{-1} $F_8 = 1506.13$ cm^{-1} $F_{12} = 1497.1$ cm^{-1} $F_{14} = 1488.98$ cm^{-1}. Comparing the integral area ratio (A_{sp}^3/A_{sp}^2) of sp^3 and sp^2, we can obtain $A_8(0.32) > A_{14}(0.302) > A_{12}(0.186)$, and A_{12} has the smallest integral area, indicating that the sp^2 carbon exists in the sample with the highest amount of carbon in 12 h. The sp^2 hybridized carbon atoms have high p-orbital overlap and π-electron conjugation effects, so the more carbon atoms there are in the sp^2 type, the more space and electronic effects can be provided for the catalytic process, which is more favorable to the catalytic process.[33] For the representation of the D and G peaks present in the Raman test, the D peak corresponds to the location of the defect, while the G peak belongs to the graphite pattern. The appearance of the D peak may originate from amorphous carbon, graphite, nanoparticles, and nanoscale microcrystals. The ratio of I_D/I_G (intensity ratio) in the three groups of samples is $I_8 = 1.33$, $I_{12} = 1.44$, $I_{14} = 1.4$, indicating that the carbon atoms in the 12 h sample group have the most crystal defects, which is also consistent with the peak intensity of C=O in the XPS analysis. Similarly, the I_D/I_G value is inversely proportional to the effective crystallite size in the direction of the graphite plane (La), and the larger the value, the lower the degree of graphitization, so ZIF8/ZnO-12 has the lowest degree of graphitization, and the combination of the XRD and electron microscopy results shows that the product is mainly amorphous structure.

Fig. S1† displays SEM images of ZnO nanostructures synthesized *via* water bath heating for varying durations. Specifically, Fig. S1(a and b)† exhibit ZnO-8 synthesized for 8 hours, characterized by a snowflake-like morphology with nanorods having an average diameter of approximately 200–300 nm. Fig. S1(c and d)† depict ZnO-12 synthesized over 12 hours, showcasing a dispersed arrangement of nanorods with an average diameter ranging from 100–200 nm. Lastly, Fig. S1(e and f)† indicate that the majority of crystals synthesized in 14 hours consist of a mixture of incompletely
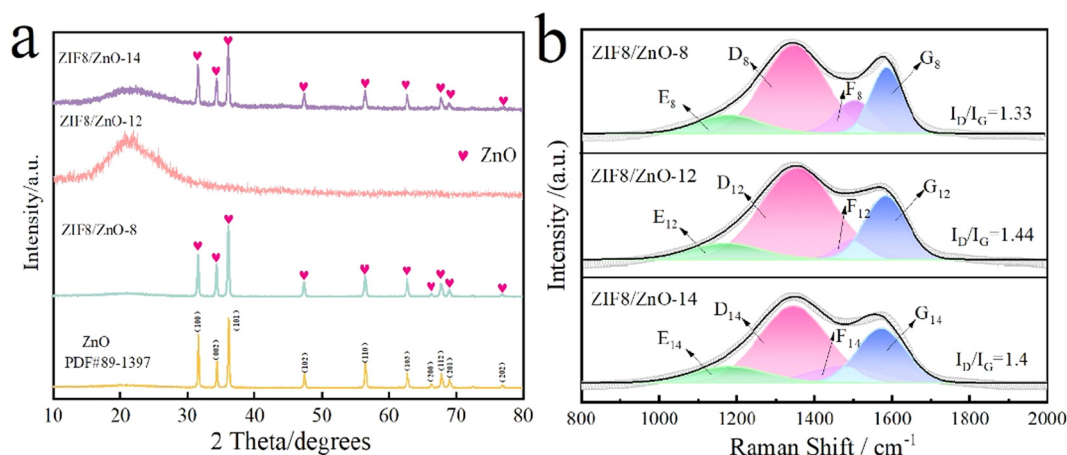

Fig. 1   XRD pattern of catalyst prepared at different reaction times (a) Raman analysis diagram (b).

formed hollow nanotubes with an average diameter of about 600–900 nm, along with nanotubes having an average diameter of approximately 300 nm.

Fig. 2(a–f) displays the SEM images of the catalyst after pyrolysis at 800 °C. Specifically, Fig. 2(a and d) illustrate the pyrolysis of ZnO-8 floral nanorods after attachment of ZIF8, revealing that some of the nanorods began to break and the nanoflowers dispersed. Fig. 2(b and e) show the pyrolysis of ZnO-12 nanorods attached to ZIF8, where the hexagonal structure of ZIF8 is clearly visible. The overall layered network structure exhibits a higher surface area, which is beneficial for ion transport. Fig. 2(c and f) present the SEM image of ZIF8/ZnO-14, which exhibits more nanorods with a less layered

structure. Fig. 2(g–i) exhibit the TEM images of ZIF8/ZnO-8, ZIF8/ZnO-12, and ZIF8/ZnO-14, respectively. The dark blocks appearing in Fig. 2(k) indicate that ZIF8/ZnO-8 has not been fully carbonized at this temperature. When compared with the XRD results, it is evident that the dark masses are ZnO. Consequently, the ZIF8/ZnO-12 sample has the highest degree of carbonization with almost no visible ZnO; ZIF8/ZnO-14 contains some dark ZnO lumps and demonstrates moderate carbonization; while ZIF8/ZnO-8 has the poorest degree of carbonization. Fig. 2(j and k) present the SEM and TEM images of ZIF8/ZnO-12 before pyrolysis. Similarly, ZIF8/ZnO-8 and ZIF8/ZnO-14 exhibit analogous structural characteristics, collectively indicating that ZIF8 has achieved complete coating of the ZnO
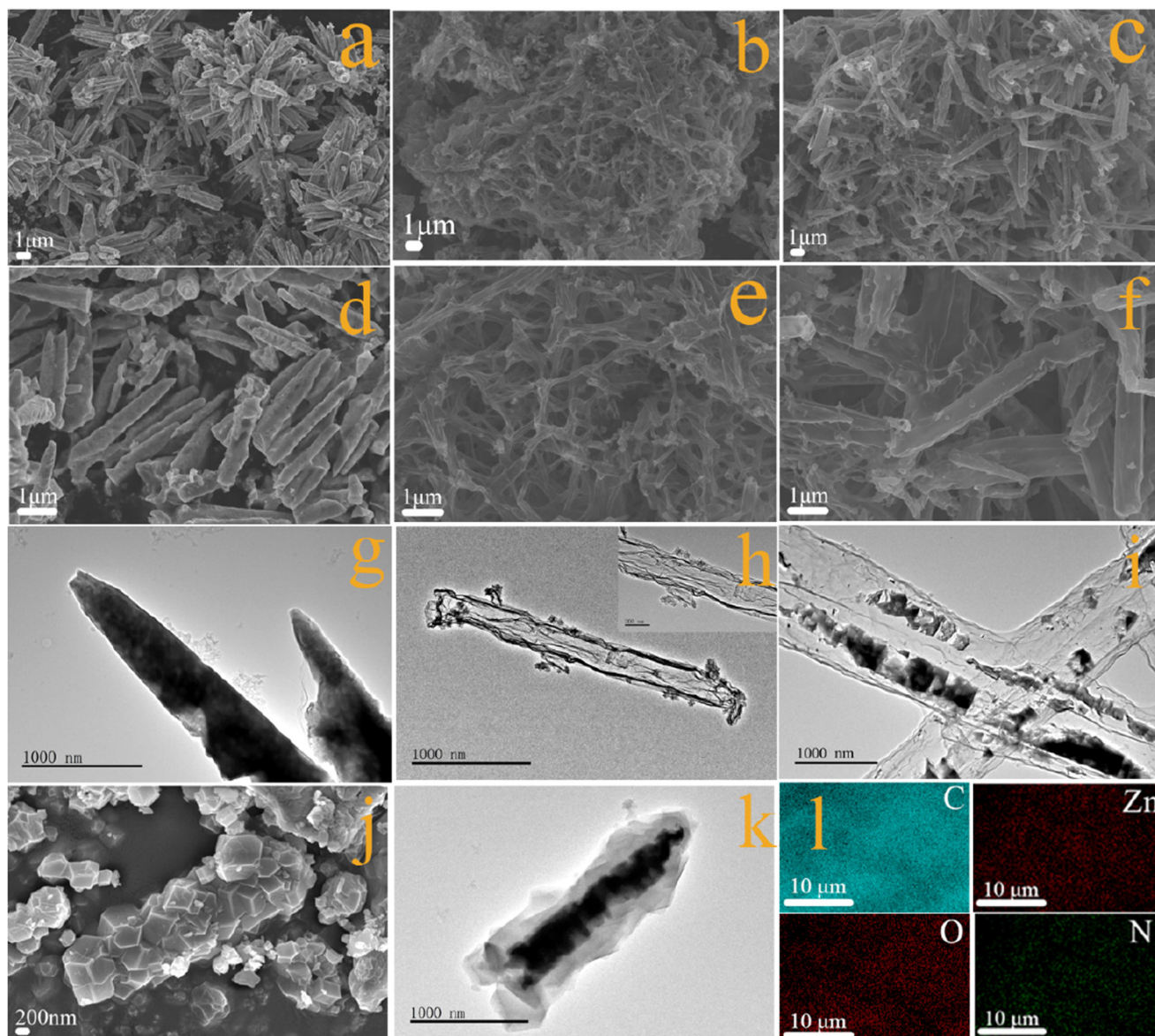

Fig. 2 (a and d) SEM images of ZIF8/ZnO-8; (b and e) SEM images of ZIF8/ZnO-12; (c and f) SEM images of ZIF8/ZnO-14; (g) TEM image of ZIF8/ZnO-8; (h) TEM image of ZIF8/ZnO-12; (i) TEM image of ZIF8/ZnO-14; (j) SEM image of ZIF8/ZnO-12 before pyrolysis; (k) T ZIF8/ZnO-12 before pyrolysis; (l) elemental mapping diagram C, Zn, O, N corresponding to ZIF8/ZnO-12 ZIF8/ZnO-12 before pyrolysis.

nanoparticles. This observation suggests a consistent and thorough coating process across the different ZnO samples. And in Fig. 2(l), along with ESI Fig. S3 and Table S1,† EDS spectroscopy and related compositional analyses demonstrate that the most highly carbonized ZIF8/ZnO-12 sample contains elements of C, O, N, and Zn. The major component, C, accounts for 93.34% of the carbonized ZIF8/ZnO-12 sample, while the atomic percentage of Zn is only 0.23%. This is consistent with the XRD test results and further suggests that the ZIF8/ZnO-12 sample has been nearly completely carbonized. ESI Fig. S2(a and b)† displays the HRTEM image of ZIF8/ZnO-12, indicating that the material is amorphous, with a significant amount of amorphous regions and a small amount of graphite microcrystalline regions.

Fig. 3(a) shows the full XPS spectra of ZIF8/ZnO-8, ZIF8/ZnO-12, and ZIF8/ZnO-14, indicating that the prepared catalytic materials contain elements of Zn, O, C, and N. The high-resolution XPS of C 1s in the sample in Fig. 3(b) could be divided into four peaks after fitting analysis.[34–36] corresponding to C–C (284.36, 284.17 and 284.36 eV); C–N (285.27, 285.14 and 285.15 eV); C–O (286.11, 286.07 and 286.05 eV); C═O (288.65, 288.16 and 288.03 eV). The appearance of C–N shows that the nitrogen in 2-methylimidazole is successfully doped into the amorphous carbon. The peaks appearing for C–O and C═O are due to the chemisorption of oxygen molecules from air through the dangling bonds on the defects on the surface of the amorphous carbon.[37] The C═O peak in ZIF8/ZnO-12 is significantly stronger than that in ZIF8/ZnO-8 and ZIF8/ZnO-14, indicating that the 12 h sample set has the most abundant crystal defects of carbon atoms, which is in agreement with the results of Raman analysis. About O 1s spectrum in Fig. 3(c) reveals three chemical states. O_1, which belongs to the lattice oxygen in ZnO,[38] corresponds to peaks at 530.64 eV, 530.41 eV, and 530.75 eV. O_2 is noted as oxygen vacancies, corresponding to peaks at 531.25 eV, 531.43 eV, and 531.59 eV. O_3 is noted as oxygen bound to carbon, with peaks at 532.12 eV, 532.83 eV, and 532.83 eV.[39] Fig. 3(d) is about N 1s,[40,41] with peaks at 398.15, 397.84 and 398.19 eV corresponding to pyridine N on each catalyst, peaks at 399.85, 399.58 and 399.84 eV corresponding to pyrrole N on each catalyst, and peaks at 400.86, 400.64 and 400.85 eV corresponding to graphite N. The results further indicate the successful doping of nitrogen atoms in the carbon layer. Among them, the peak area of pyridine-N has the largest percentage, which leads to the conclusion that nitrogen doping is mainly in the form of pyridine-N. In the most highly carbonized ZIF8/ZnO-12 sample, graphitic N exhibits the smallest peak area, and the lower graphitic N content indicates the higher purity of the
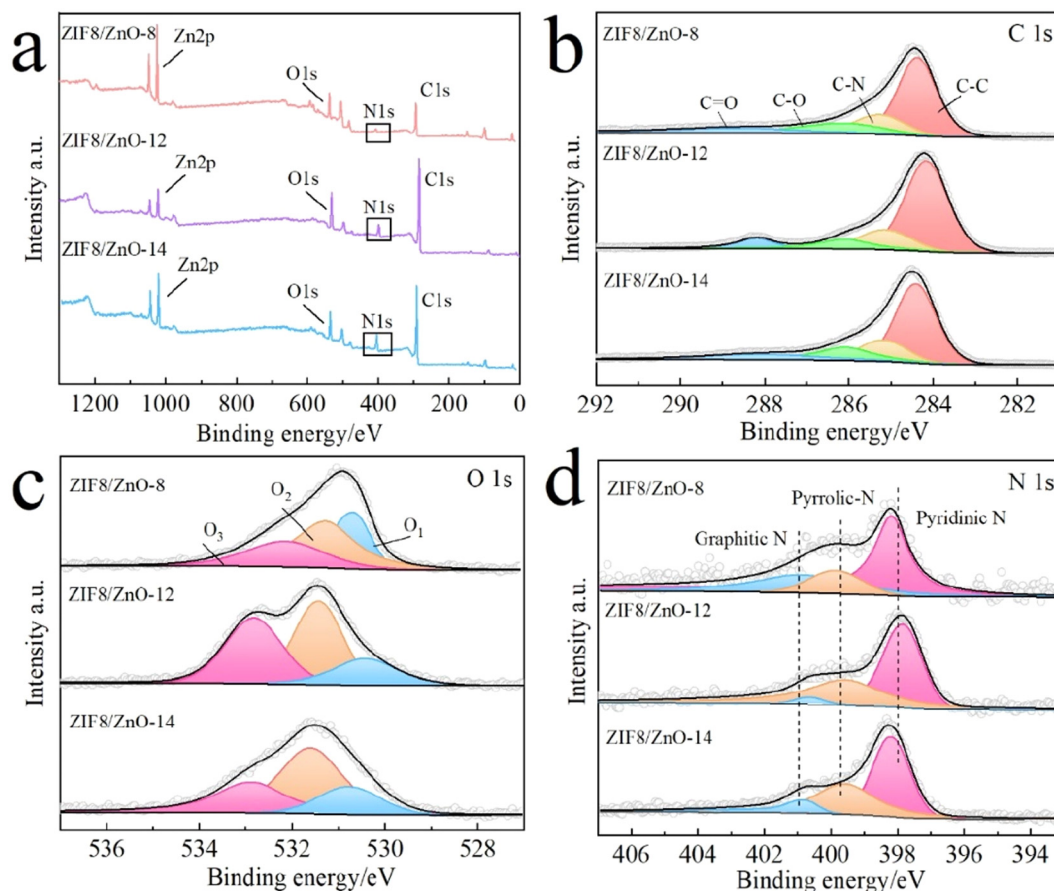

Fig. 3 (a) Full spectrum; (b) C 1s; (c) O 1s; (d) N 1s XPS spectrum.

catalyst. The XPS spectrum of Zn 2p is shown in Fig. S4,†[42] with three fitted peaks appearing at 1022.06 and 1045.09 eV; 1021.27 and 1044.32 eV; 1021.61 and 1044.61 eV, respectively belonging to Zn $2p_{1/2}$ and Zn $2p_{3/2}$. Furthermore, the binding energy distance between each pair of peaks is 23 eV, again in accordance with the standard reference value for ZnO.

To investigate the ORR performance of the catalysts obtained, the ORR catalytic performance of ZIF8/ZnO-8, ZIF8/ZnO-12, and ZIF8/ZnO-14 was evaluated in a 0.1M KOH electrolyte that is saturated with N_2/O_2. In the CV test, as shown in Fig. 4(a), a smooth voltammogram (*vs.* RHE) was noted in the voltage range from −0.1 V to +1.1 V under N_2 saturated con-
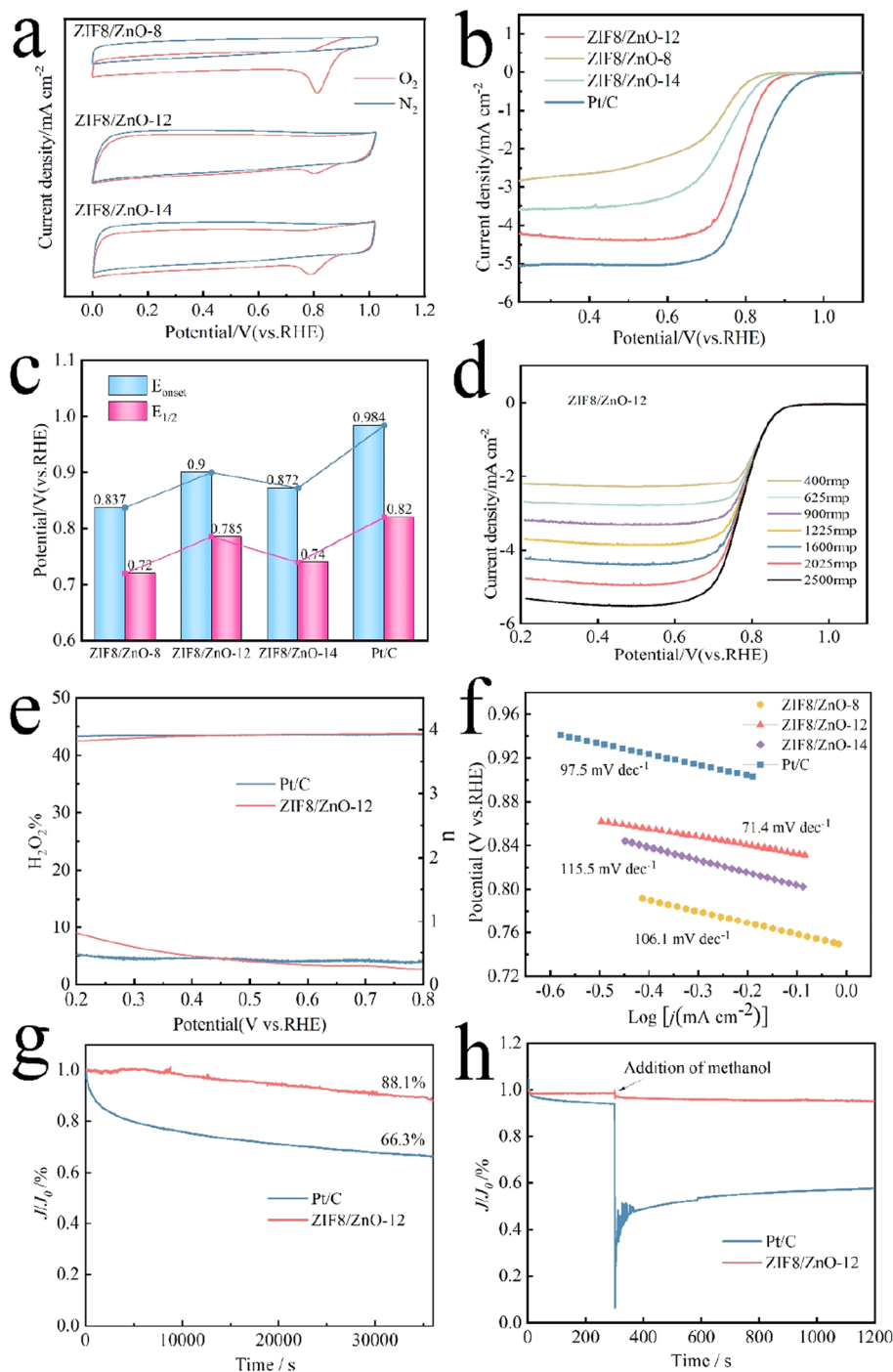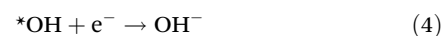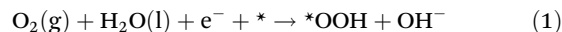

Fig. 4 (a) CV curves of different catalysts under O_2/N_2 saturation conditions; (b) LSV curves of various catalysts at 1600 rpm; (c) comparative statistical diagram of various catalysts at E_{onset}, $E_{1/2}$; (d) LSV curves at different speeds; (e) RRDE method to test the transfer of electrons and the yield of H_2O_2; (f) Tafel curve; (g) stability test; (h) methanol poisoning resistance test.

ditions, but sharp redox peaks were observed in O_2 saturated 0.1 M KOH solution, which suggests that each catalyst exhibits significant ORR electrocatalytic activity in alkaline media. Fig. 4(b) presents the RDE electrochemical tests performed on each catalyst to assess the catalytic behavior, and Fig. 4(c) presents the statistical plot of the initial potential and half-wave potential, combined with Fig. 4(b). The linear scan curve shows that ZIF8/ZnO-12 exhibits $E_{onset} = 0.9$ V, $E_{1/2} = 0.785$ V, $J_L = -4.39$ mA cm^{-2} at 1600 rpm; ZIF8/ZnO-8 exhibits $E_{onset} = 0.837$ V, $E_{1/2} = 0.72$ V; ZIF8/ZnO-14 exhibits $E_{onset} = 0.872$ V, $E_{1/2} = 0.74$ V. ZIF8/ZnO-12, as the sample with the highest degree of carbonization, exhibits excellent ORR activity in carbon materials. To further evaluate the ORR kinetics of the sample, Fig. 4(d) shows the RRDE measurements on the ZIF8/ZnO-12 modified glassy carbon electrode. O_2 saturated 0.1 M KOH solution at different speeds from 400 to 2500 rpm with a scan rate of 10 mV s^{-1}. The faster the speed, the faster the O_2 diffusion to the catalyst surface and the current density increases with the speed.

Selectivity and stability are also important in the evaluation of ORR performance. As shown in Fig. 4(e), the intermediate product H_2O_2 yield of ZIF8/ZnO-12 is low and the electron transfer number is close to 4 electron transfers, which is similar to the performance of Pt/C catalyst. The Tafel comparison diagram was made using the second-order differential method, as shown in Fig. 4(f). The Tafel slope corresponding to ZIF8/ZnO-12 was 71.4 mV dec^{-1}, which was lower than that of Pt/C catalyst (97.5 mV dec^{-1}), ZIF8/ZnO-8 (106.1 mV dec^{-1}) and ZIF8/ZnO-14 (115.5 mV dec^{-1}), indicating that ZIF8/ZnO-12 was favorable for producing better dynamic processes. Fig. 4(g) shows the chronoamperometric (I–t) curve. After 36 000 seconds of sequential testing, the current density of Pt/C and ZIF8/ZnO-12 decreased to 66.3% and 88.1%, respectively. The experimental results showed that ZIF8/ZnO-12 had good ORR stability. The tolerance of ZIF8/ZnO-12 and Pt/C to methanol was shown in Fig. 4(h). After adding 2 M methanol to the electrode after 300 s, the current density of ZIF8/ZnO-12 showed almost no change, while the current density of commercial Pt/C, on the other hand, drops dramatically, indicating that ZIF8/ZnO-12 had good methanol tolerance.

Furthermore, to assess the viability of the ZIF8/ZnO-12 catalyst in zinc-air environments, the cathode catalyst is loaded at 0.8 mg cm^{-2} in the zinc-air battery. ZABs based on ZIF8/ZnO-12 exhibit a higher open-circuit voltage of 1.56 V, gradually decreasing to a stable value of 1.53 V after an equilibrium process lasting 1800 seconds, comparable to the stable value reached by Pt/C during the same period in Fig. S5.† Polarization curves and power density are illustrated in Fig. 5(a), where the ZIF8/ZnO-12 catalyst demonstrates a peak power density of 103.1 mW cm^{-2} at a current density of 159.7 mA cm^{-2}. This value is slightly lower compared to Pt/C its peak power density counterpart (169.8 mA cm^{-2}, 122 mW cm^{-2}). Fig. 5(b) displays discharge curves at a constant current of 10 mA cm^{-2}, and the calculated specific capacity for ZIF8/ZnO-12 is 816 mA h g^{-1}, surpassing that of Pt/C (770 mA h g^{-1}).

Although ZIF8/ZnO-12 exhibits excellent electrochemical performance, the binding of C and O in XPS analysis cannot intuitively reveal the contribution of different types of O to ORR. Here, we design an atomic model of pyridinic nitrogen binding with O to replace graphene, and the relevant calculation methods are shown in Fig. S7.† The binding of O is considered in three cases: adsorption of O, doping of O, and co-doping of O and adsorption of O.[43] This is done to compare the differences in catalytic activity of different catalysts. The changes in the ORR free energy of these catalysts at $U = 0$ V and equilibrium potential of the alkaline environment, $U = 0.460$ V (0.1 mol L^{-1} KOH), were investigated using DFT, as shown in Fig. 6(a, c and e). ORR consists of four fundamental steps:

$$O_2(g) + H_2O(l) + e^- + * \rightarrow *OOH + OH^- \tag{1}$$

$$*OOH + e^- \rightarrow *O + OH^- \tag{2}$$

$$*O + H_2O(l) + e^- \rightarrow *OH + OH^- \tag{3}$$

$$*OH + e^- \rightarrow OH^- \tag{4}$$

The corresponding atomic configurations of ORR intermediates are shown in Fig. 6(b, d and f). For the whole reaction pathway of pyridinic nitrogen adsorbed O-substituted graphene. It can be seen that the formation of OOH* intermedi-
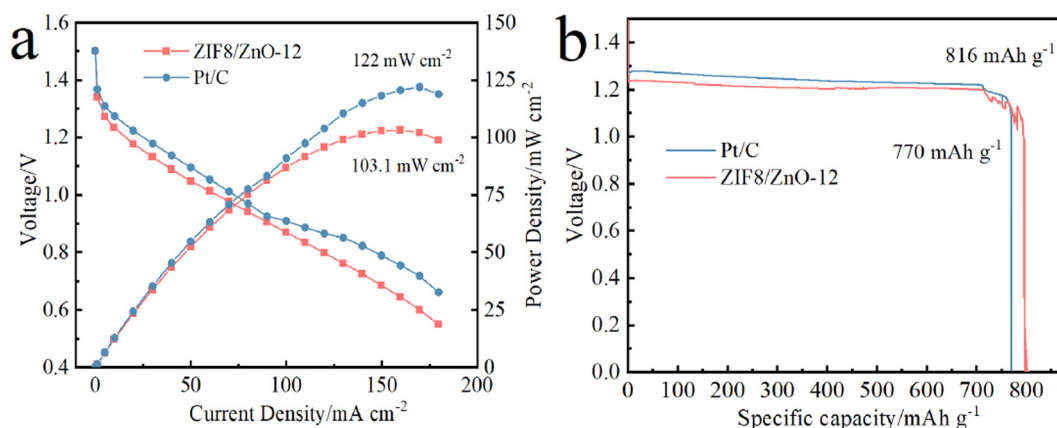

Fig. 5 (a) Power density of ZIF8/ZnO-12 and Pt/C; (b) discharge curves of ZIF8/ZnO-12 and Pt/C at 10 mA cm^{-2}.
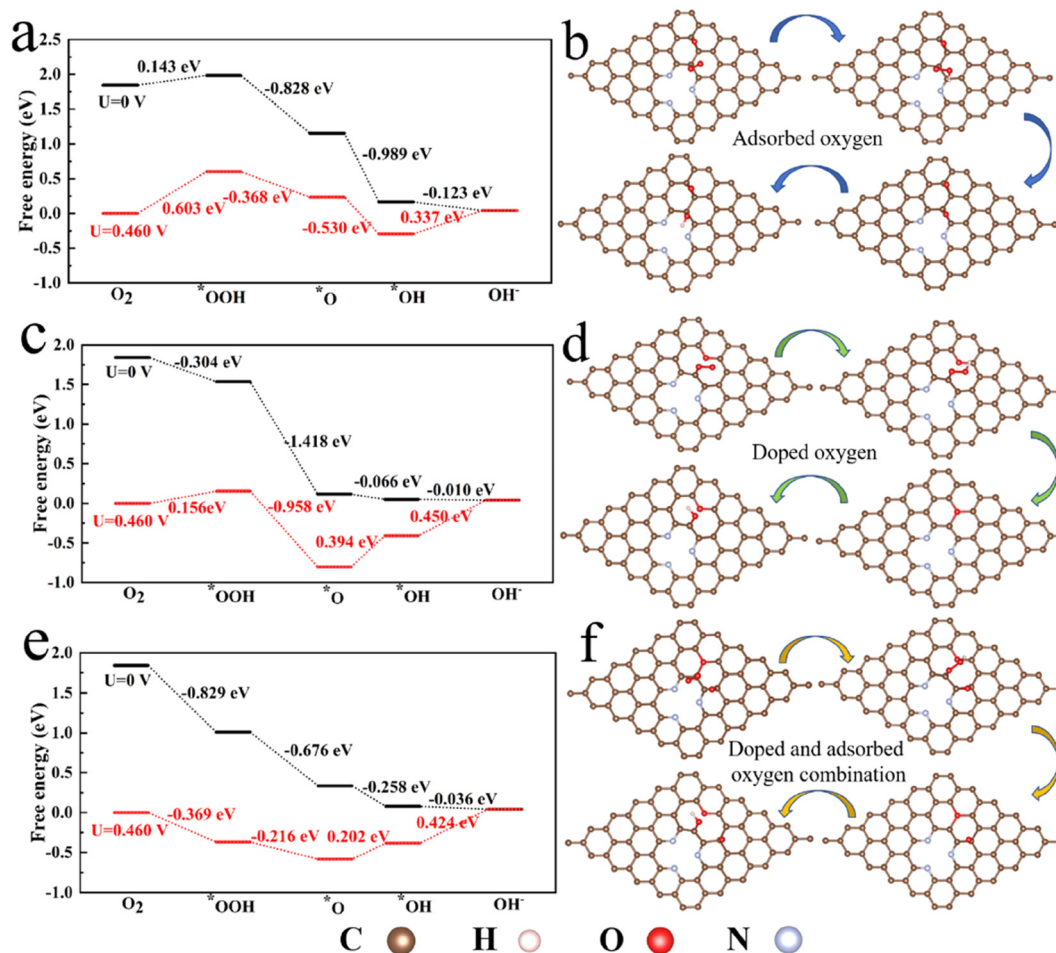
Fig. 6 (a, c and e) Changes in ORR reaction free energy of adsorbed O, doped O, and doped-adsorbed O combined catalysts; (b, d and f) atomic configuration diagrams of ORR intermediate states corresponding to adsorbed O, doped O, and doped-adsorbed O binding catalysts.

ates has the highest change in uphill free energy, which is the decisive step of the reaction. O_2 molecules are difficult to be adsorbed on pyridine N-graphene, which is consistent with previous reports.[44,45] For both pyridinic nitrogen doped O-substituted graphene and Pyridinic nitrogen adsorbed co-doped O-substituted graphene, the decisive step is the desorption of the last OH*. The change in the rate-determining step may be attributed to the fact that doping of O is more likely to alter the charge distribution of the catalyst substrate compared to adsorption of O, thereby modifying the catalytic performance of the catalyst. The C atoms near O adsorption/doping are considered as the active sites for the ORR, while the C atoms adjacent to N, due to steric hindrance, do not serve as adsorption active sites. However, the reactivity of these active C atoms is influenced by the positively charged adjacent C atoms.[46] Comparing the free energy changes of the rate-determining steps for three catalysts: adsorption of O, doping of O, co-doping of O and adsorption of O, it is evident that under alkaline conditions (U = 0.460 V), the catalytic activity of pyridinic nitrogen doped O-substituted graphene (0.450 eV) and pyridinic nitrogen adsorbed co-doped O-substituted graphene

(0.424 eV) is significantly higher than that of pyridinic nitrogen adsorbed O-substituted graphene (0.603 eV). The former two are more likely to undergo ORR.

4. Conclusion

ZnO nanomaterials of varying tube diameters are being synthesized *via* a reproducible water bath method, adjusting reaction time, and integrated with ZIF-8 using a diameter control strategy. We're studying how reaction time affects product structure and its subsequent impact on the oxygen reduction reaction in electrocatalysis. ZnO-12 nanotubes, noted for their narrow diameters, undergo complete carbonization at 800 °C, releasing zinc ions and forming an amorphous carbon nano-hollow structure, ZIF8/ZnO-12. Electrochemical tests reveal an impressive E_{oneset} of 0.9 V (*vs.* RHE), outperforming Pt/C's Tafel slope and exhibiting remarkable stability. In zinc–air battery tests, ZIF8/ZnO-12 amorphous carbon nanomaterial demonstrates superior specific capacity to Pt/C. Raman spectroscopy shows ZIF8/ZnO-12 has the highest proportion of sp²

hybridized carbon atoms, enhancing catalytic processes through spatial and electronic effects. XPS analysis indicates carbon atoms with more crystal defects. DFT calculations suggest that co-doping and adsorption of oxygen favor the ORR. This experimental design preserves amorphous carbon's structure while lowering the pyrolysis temperature, improving catalytic efficiency. This approach holds tremendous economic potential for cost-effective carbon-based catalysts, crucial for environmental sustainability and resource recirculation.

Data availability

The raw/processed data required to reproduce these findings cannot be shared at this time as the data also forms part of an ongoing study.

Conflicts of interest

There are no conflicts to declare.

Acknowledgements

References

1 K. Gong, F. Du, Z. Xia, M. Durstock and L. Dai, Nitrogen-Doped Carbon Nanotube Arrays with High Electrocatalytic Activity for Oxygen Reduction, *Science*, 2009, **323**, 760–764.

2 J. Zhang, Z. Zhao, Z. Xia and L. Dai, A metal-free bifunctional electrocatalyst for oxygen reduction and oxygen evolution reactions, *Nat. Nanotechnol.*, 2015, **10**, 444–452.

3 H. Yu, L. Shang, T. Bian, R. Shi, G. I. N. Waterhouse, Y. Zhao, C. Zhou, L.-Z. Wu, C.-H. Tung and T. Zhang, Nitrogen-Doped Porous Carbon Nanosheets Templated from g-C3N4 as Metal-Free Electrocatalysts for Efficient Oxygen Reduction Reaction, *Adv. Mater.*, 2016, **28**, 5080–5086.

4 H.-W. Liang, X. Zhuang, S. Brüller, X. Feng and K. Müllen, Hierarchically porous carbons with optimized nitrogen doping as highly active electrocatalysts for oxygen reduction, *Nat. Commun.*, 2014, **5**, 4973.

5 K. Sakaushi, A. Lyalin, S. Tominaka, T. Taketsugu and K. Uosaki, Two-Dimensional Corrugated Porous Carbon-, Nitrogen-Framework/Metal Heterojunction for Efficient Multielectron Transfer Processes with Controlled Kinetics, *ACS Nano*, 2017, **11**, 1770–1779.

6 T. Fukushima, W. Drisdell, J. Yano and Y. Surendranath, Graphite-Conjugated Pyrazines as Molecularly Tunable Heterogeneous Electrocatalysts, *J. Am. Chem. Soc.*, 2015, **137**, 10926–10929.

7 D. Guo, R. Shibuya, C. Akiba, S. Saji, T. Kondo and J. Nakamura, Active sites of nitrogen-doped carbon materials for oxygen reduction reaction clarified using model catalysts, *Science*, 2016, **351**, 361–365.

8 X. Huang, Y. Wang, W. Li and Y. Hou, Noble metal-free catalysts for oxygen reduction reaction, *Sci. China: Chem.*, 2017, **60**, 1494–1507.

9 W. He, Y. Wang, C. Jiang and L. Lu, Structural effects of a carbon matrix in non-precious metal O2-reduction electrocatalysts, *Chem. Soc. Rev.*, 2016, **45**, 2396–2409.

10 I.-Y. Jeon, H.-J. Choi, M. J. Ju, I. T. Choi, K. Lim, J. Ko, H. K. Kim, J. C. Kim, J.-J. Lee, D. Shin, S.-M. Jung, J.-M. Seo, M.-J. Kim, N. Park, L. Dai and J.-B. Baek, Direct nitrogen fixation at the edges of graphene nanoplatelets as efficient electrocatalysts for energy conversion, *Sci. Rep.*, 2013, **3**, 2260.

11 A. Shen, Y. Zou, Q. Wang, R. A. W. Dryfe, X. Huang, S. Dou, L. Dai and S. Wang, Oxygen Reduction Reaction in a Droplet on Graphite: Direct Evidence that the Edge Is More Active than the Basal Plane, *Angew. Chem., Int. Ed.*, 2014, **53**, 10804–10808.

12 J. Biemolt, G. Rothenberg and N. Yan, Understanding the roles of amorphous domains and oxygen-containing groups of nitrogen-doped carbon in oxygen reduction catalysis: toward superior activity, *Inorg. Chem. Front.*, 2020, **7**, 177–185.

13 E. F. Sheka, Y. A. Golubev and N. A. Popova, Amorphous state of sp2 solid carbon, *Fullerenes, Nanotubes Carbon Nanostruct.*, 2020, **29**, 107–113.

14 P. Trogadas, T. F. Fuller and P. Strasser, Carbon as catalyst and support for electrochemical energy conversion, *Carbon*, 2014, **75**, 5–42.

15 S. Zhao, D. W. Wang, R. Amal and L. Dai, Carbon-Based Metal-Free Catalysts for Key Reactions Involved in Energy Conversion and Storage, *Adv. Mater.*, 2018, **31**, 1801526.

16 Y. Yao, H. Wu, L. Huang, X. Li, S. Yu, S. Zeng, X. Zeng, J. Yang and J. Zou, Nitrogen-enriched hierarchically porous carbon nanofiber network as a binder-free electrode for high-performance supercapacitors, *Electrochim. Acta*, 2017, **246**, 606–614.

17 L. Cao, Z. Lin, J. Huang, X. Yu, X. Wu, B. Zhang, Y. Zhan, F. Xie, W. Zhang, J. Chen, W. Xie, W. Mai and H. Meng, Nitrogen doped amorphous carbon as metal free electrocatalyst for oxygen reduction reaction, *Int. J. Hydrogen Energy*, 2017, **42**, 876–885.

18 H. Deng, Z. Wang, M. Kim, Y. Yamauchi, S. J. Eichhorn, M.-M. Titirici and L. Deng, Unleashing the power of capacitive deionization: Advancing ion removal with biomass-derived porous carbonaceous electrodes, *Nano Energy*, 2023, **117**, 108914.

19 L. Chai, L. Zhang, X. Wang, L. Xu, C. Han, T.-T. Li, Y. Hu, J. Qian and S. Huang, Bottom-up synthesis of MOF-derived hollow N-doped carbon materials for enhanced ORR performance, *Carbon*, 2019, **146**, 248–256.

20 Q. Sun, D. Chen, Q. Huang, S. Huang and J. Qian, Carbon nanotubes anchored onto hollow carbon for efficient oxygen reduction, *Sci. China Mater*, 2023, **66**, 641–650.

21 S. Xu, A. Dong, Y. Hu, Z. Yang, S. Huang and J. Qian, Multidimensional MOF-derived carbon nanomaterials for multifunctional applications, *J. Mater. Chem. A*, 2023, **11**, 9721–9747.

22 J. Zou, P. Liu, L. Huang, Q. Zhang, T. Lan, S. Zeng, X. Zeng, L. Yu, S. Liu, H. Wu, W. Tu and Y. Yao, Ultrahigh-content nitrogen-decorated nanoporous carbon derived from metal organic frameworks and its application in supercapacitors, *Electrochim. Acta*, 2018, **271**, 599–607.

23 B. Hwang, S.-H. Yi and S.-E. Chun, Dual-role of ZnO as a templating and activating agent to derive porous carbon from polyvinylidene chloride, PVDC, resin, *Chem. Eng. J.*, 2021, **422**, 130047.

24 B. Huang, W. Zeng and Y. Li, Synthesis of ZIF-8 Coating on ZnO Nanorods for Enhanced Gas-Sensing Performance, *Chemosensors*, 2022, **10**, 297.

25 A. Kaphle, T. Reed, A. Apblett and P. Hari, Doping Efficiency in Cobalt-Doped ZnO Nanostructured Materials, *J. Nanomater.*, 2019, **2019**, 1–13.

26 Z. Cui, Y. Xue, L. Xiao and T. Wang, Effect of Particle Size on Activation Energy for Thermal Decomposition of Nano-$CaCO_3$, *J. Comput. Theor. Nanosci.*, 2013, **10**, 569–572.

27 R. Saibal, B. T. Kumar, V. K. Kumar, D. Debabrata, G. Shounak and D. Santanu, Non-isothermal decomposition kinetics of nano-scale $CaCO_3$ as a function of particle size variation, *Ceram. Int.*, 2021, **47**, 858–864.

28 L. Jiang, X.-R. Yang, X. Gao, Q. Xu, O. Das, J.-H. Sun and M. K. Kuzman, Pyrolytic Kinetics of Polystyrene Particle in Nitrogen Atmosphere: Particle Size Effects and Application of Distributed Activation Energy Method, *Polymers*, 2020, **12**, 421.

29 K. A. Bustos-Torres, S. Vazquez-Rodriguez, A. M.-d. la Cruz, S. Sepulveda-Guzman, R. Benavides, R. Lopez-Gonzalez and L. M. Torres-Martínez, Influence of the morphology of ZnO nanomaterials on photooxidation of polypropylene/ZnO composites, *Mater. Sci. Semicond. Process.*, 2017, **68**, 217–225.

30 Y.-S. Tsai, J.-R. Chen, C.-H. Lee, C.-C. Kuo, Y.-H. Lin, C.-C. Wang, Y.-C. Chang, Y. S. Wu and H. Chen, Morphologies and material properties of ZnO nanotubes, ZnO/ZnS core-shell nanorods, and ZnO/ZnS core-shell nanotubes, *Ceram. Int.*, 2022, **48**, 7232–7239.

31 B. Huang, W. Zeng and Y. Li, Synthesis of ZnO@ZIF-8 Nanorods with Enhanced Response to VOCs, *J. Electrochem. Soc.*, 2022, **169**, 047508.

32 P.-C. Shi, J.-D. Yi, T.-T. Liu, L. Li, L.-J. Zhang, C.-F. Sun, Y.-B. Wang, Y.-B. Huang and R. Cao, Hierarchically porous nitrogen-doped carbon nanotubes derived from core–shell ZnO@zeolitic imidazolate framework nanorods for highly efficient oxygen reduction reactions, *J. Mater. Chem. A*, 2017, **5**, 12322–12329.

33 S. J. Yang, T. Kim, J. H. Im, Y. S. Kim, K. Lee, H. Jung and C. R. Park, MOF-Derived Hierarchically Porous Carbon with Exceptional Porosity and Hydrogen Storage Capacity, *Chem. Mater.*, 2012, **24**, 464–470.

34 Z. Wu and X.-B. Zhang, N,O-codoped porous carbon nanosheets for capacitors with ultra-high capacitance, *Sci. China Mater*, 2016, **59**, 547–557.

35 Z. Zhou, K. Zhang, J. Liu, H. Peng and G. Li, Comparison study of electrochemical properties of porous zinc oxide/N-doped carbon and pristine zinc oxide polyhedrons, *J. Power Sources*, 2015, **285**, 406–412.

36 Z. Zhang, G. Li, H. Peng and K. Chen, Hierarchical hollow microspheres assembled from N-doped carbon coated Li4Ti5O12 nanosheets with enhanced lithium storage properties, *J. Mater. Chem. A*, 2013, **1**, 15429.

37 C. Tang, C. Chen, H. Zhang, J. Zhang and Z. Li, Enhancement of degradation for nitrogen doped zinc oxide to degrade methylene blue, *Phys. B*, 2020, **583**, 412029.

38 X. Q. Wei, B. Y. Man, M. Liu, C. S. Xue, H. Z. Zhuang and C. Yang, Blue luminescent centers and microstructural evaluation by XPS and Raman in ZnO thin films annealed in vacuum, N2 and O2, *Phys. B*, 2007, **388**, 145–152.

39 Y. Sun, H. Xiao, H. Li, Y. He, Y. Zhang, Y. Hu, Z. Ju, Q. Zhuang and Y. Cui, Nitrogen/Oxygen Co–Doped Hierarchically Porous Carbon for High–Performance Potassium Storage, *Chem. – Eur. J.*, 2019, **25**, 7359–7365.

40 Y. Yin, B. Hu, G. Liu, X. Zhou and X. Hong, ZnO@ZIF-8 Core-Shell Structure as Host for Highly Selective and Stable Pd/ZnO Catalysts for Hydrogenation of CO_2 to Methanol, *Acta Phys.-Chim. Sin.*, 2019, **35**, 327–336.

41 E. Samuel, B. Joshi, M.-W. Kim, Y.-I. Kim, S. Park, T.-G. Kim, M. T. Swihart, W. Y. Yoon and S. S. Yoon, Zeolitic imidazolate framework-8 derived zinc oxide/carbon nanofiber as freestanding electrodes for lithium storage in lithium-ion batteries, *J. Power Sources*, 2018, **395**, 349–357.

42 X. Zeng, Z. Yang, F. Cui, L. Chen, J. Meng and H. Chen, The dodecahedral Nitrogen-doped carbon coated ZnO composite derived from zeolitic inidazolate framework-8 with excellent cycling performance for zinc based rechargeable batteries, *J. Power Sources*, 2020, **463**, 228193.

43 X. Zhu, K. Liu, Z. Lu, Y. Xu, S. Qi and G. Zhang, Effect of oxygen atoms on graphene: Adsorption and doping, *Phys. E*, 2020, **117**, 113827.

44 X. Zou, L. Wang and B. I. Yakobson, Mechanisms of the oxygen reduction reaction on B- and/or N-doped carbon nanomaterials with curvature and edge effects, *Nanoscale*, 2018, **10**, 1129–1134.

45 C. H. Choi, H.-K. Lim, M. W. Chung, J. C. Park, H. Shin, H. Kim and S. I. Woo, Long-Range Electron Transfer over Graphene-Based Catalyst for High-Performing Oxygen Reduction Reactions: Importance of Size, N-doping, and Metallic Impurities, *J. Am. Chem. Soc.*, 2014, **136**, 9070–9077.

46 Q. Lv, W. Si, J. He, L. Sun, C. Zhang, N. Wang, Z. Yang, X. Li, X. Wang, W. Deng, Y. Long, C. Huang and Y. Li, Selectively nitrogen-doped carbon materials as superior metal-free catalysts for oxygen reduction, *Nat. Commun.*, 2018, **9**, 3376.